university of groningen / faculty of mathematics and natural sciences

Vibrational Spectroscopy of Hybrid Materials

Optical Condensed Matter Physics

Bachelor thesis June 2013

Author: S.Y. Ong

Supervisor 1: Dr. M.S. Pchenitchnikov
Supervisor 2: Prof.dr.ir. P.H.M. van Loosdrecht

Vibrational Spectroscopy of Hybrid Materials

Yori Ong

June 24, 2013

Abstract

The perovskite inorganic-organic hybrid material $(C_6H_5CH_2CH_2NH_3)_2CuCl_4$ (=(PEA)CuCl) is known to undergo a ferroelectric phase transition at $T_c = 340$ K. A similar phase transition is expected for $(C_2H_5NH_3)_2CuCl_4$ (=(EA)CuCl) at $T_c = 356$ K. In this phase transition, an important contribution comes from order-disorder phenomena in the NH$\cdots$Cl hydrogen bond network. The objective was to investigate the vibrational spectra of (PEA)CuCl and (EA)CuCl for signs of the phase transition. It is hypothesized that rearranging of the hydrogen bond network can be seen in frequency shifts of NH stretching vibrations.

At temperatures around T_c, mid-IR spectra were recorded by means of total internal reflection and transmission infrared spectroscopy, as well as low temperature (down to 130 K) transmission spectra for both hybrids. In conclusion, the experimental methods used turned out too insensitive and inaccurate to resolve possible effects of this phase transition. If desired, a future spectroscopic study of the NH vibrations will require the effort to reduce experimental error to a minimum, as well as a more detailed insight into the origin of high frequency absorption lines.

Contents

Part I
Introduction

1 Hybrid Organic-Inorganic Materials

Hybrid organic-inorganic materials are crystal structures incorporating both organic and inorganic constituents on a molecular scale. This combination brings together useful physical properties of both the types into one material. For example, inorganic materials are associated with robustness and magnetic properties, whereas the organic materials possess chemical and structural flexibility. For this reason, hybrid materials have proven themselves useful in an increasing variety of applications [1].

Dimensionality of inorganic connectivity, I^n (n = 0–3)

Metal–organic–metal connectivity, O^n (n = 0–3)	0	1	2	3
0	Molecular complexes I^0O^0	Hybrid inorg. chains I^1O^0	Hybrid inorg. layers I^2O^0	3-D Inorg. hybrids I^3O^0
1	Chain coordination polymers I^0O^1	Mixed inorg.–organic layers I^1O^1	Mixed inorg.–organic 3-D framework I^2O^1	—
2	Layered coordination polymers I^0O^2	Mixed inorg.–organic 3-D framework I^1O^2	—	—
3	3-D Coordination polymers I^0O^3	—	—	—

Figure 1: Overview of classes of inorganic-organic hybrids. Table taken from [2]

The compact definition of organic-inorganic hybrids mentioned above still includes a large number of different materials. These can be classified based on the dimensions of connectivity of the inorganic and organic constituents. In this classification method proposed by Cheetham et al. [2], one counts the number of dimensions in which an inorganic group has infinite connectivity. This can either be an infinite connectivity with solely inorganic groups, or metal-organic-metal connectivity. Only covalent and ionic bonds are taken into account, others such as hydrogen bonds or van der Waals bonds are ignored. The class of the hybrid is denoted by the symbol I^nO^n, where I^n stands for the dimensions of inorganic connectivity and O^n represents the dimensionality of metal-organic-metal connectivity. Figure 1 shows an overview of the classes that are distinguished using this classification method.

1.1 Perovskite hybrids

In this project, the focus is placed on hybrids with the chemical formula of the type $A_2(MX_4)$. Here, A is an organic cation, M and X represent a metal and a halide respectively. The organic cation is an ammonium based structure, such as $C_6H_5C_nH_{2n}NH_3$ or $C_nH_{2n+1}NH_3$.
In these materials, the inorganic part of the structure is composed of sheets formed by corner sharing octahedra resembling a two dimensional perovskite structure. The sheets of the inorganic layer compound are interleaved by two layers of organic cations, which are oriented perpendicularly onto the inorganic sheet. The NH_3 groups of the inorganic cations form hydrogen bonds with the halide atom of the inorganic layer compound. Adjacent organic layers are connected through a Van der Waals type bonding. Following the aforementioned classification, this material concerns a hybrid inorganic layered framework (I^2O^0).
In this thesis, the focus is placed on two materials of this type: $(C_6H_5C_2H_4NH_3)_2CuCl_4$ and $(C_2H_5NH_3)_2CuCl_4$. The materials both have copper chloride as the inorganic constituent and phenylethylammonium (abbreviated: PEA) or ethylammonium (abbreviated: EA) as the organic cation. These materials will hereafter be denoted by (PEA)CuCl and (EA)CuCl respectively.

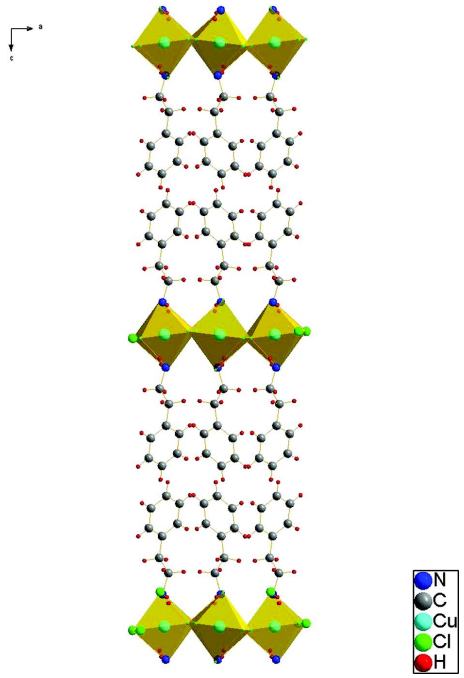

Figure 2: (PEA)CuCl structure. Image from [3]

1.2 Polar phase transition in (PEA)CuCl

This type of hybrid materials has been studied extensively in the past few decades. Among their interesting material properties are the two-dimensional magnetic ordering in the inorganic layer and a sequence of solid-state phase transitions. It was already known that (PEA)CuCl undergoes ferromagnetic ordering below 13 K . More recently it was found that this material also shows ferroelecric order below 340 K [1, 4, 3], meaning that it retains the induced polarization after removing it from an external electric field. The combination of ferromagnetic and ferroeletric ordering (and therefore multiferroicity) in a single material is of great interest for its potential applications in e.g. magnetoelectronic devices. Acquiring a detailed insight into the 340 K phase transition is one of the recent goals.
The structural phase transitions in perovskite hybrids are mostly driven by configurational changes in the organic molecules. These changes may include 'organic chain melting', reorientation of the entire organic molecule, or the flipping of the ammonium head's orientation [5, 6]. The current understanding of the phase transition in (PEA)CuCl stems from two major observations in experiments.

According to Arkenbout et al. [1, 3] a contribution to the ferroelectric behaviour can be ascribed to the ordering of hydrogen bonds that connect the inorganic and organic layers. The phase transition is driven by a change in the configuration of the inorganic perovskite layer. In the polar phase, it was shown by X-ray diffraction that the octahedra are slightly buckled with

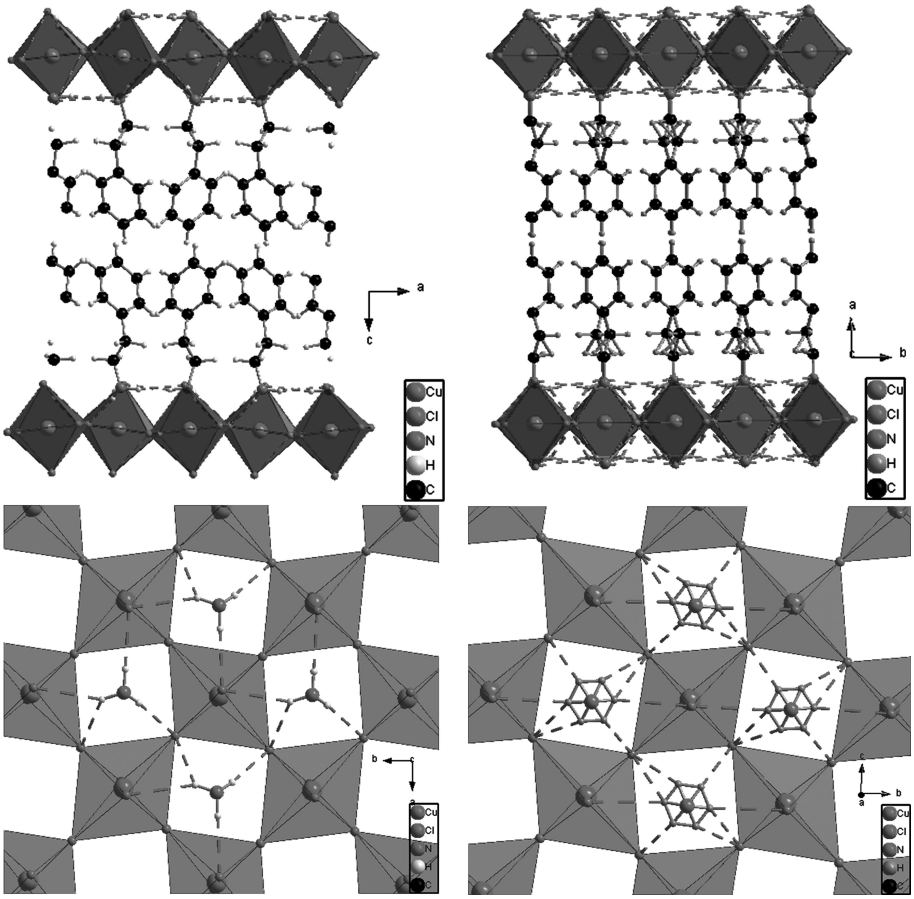

Figure 3: Schematic detail of the hydrogen bond network in (PEA)CuCl, image from ref. [1, 3]. Left: the buckling of $CuCl_6$ octahedra allows for two inequivalent ways of distributing the NH_3 hydrogen bonds. Right: After the buckling dissapears at the phase transition, both configurations become equivalent.

respect to the direction perpendicular to the layer. The buckling of the $CuCl_6$ octahedra was assigned the primary order parameter of the phase transition. The buckling creates an electromagnetic double-well potential, in which there are two stable ways to distribute the three hydrogen bonds of the cationic NH_3 group among the surrounding chlorine atoms. The first and strongest bond is in each case formed with between the top chlorine atom. The second bond however, can be linked with two inequivalent chlorine atoms, causing different displacements of the positively charged NH_3 group. The difference in displacement from a central position gives rise to a local microscopic dipole moment. Above the phase transition temperature, the buckling disappears. The symmetry of the lattice increases (from P*bca* to C*mca* space group) and no longer supports a dipole moment.

Experiments by A. Caretta [4] using temperature dependent low frequency Raman scattering have shown that the phase transition is of a mixed displacive/order-disorder type. This is backed up by the observation of a strong temperature dependence of low frequency Raman modes, assigned to librations of the organic molecule. The softening of collective escitations like these is in general a sign of a displacive phase transition. The observations agree with a tilting of the organic molecules in the polar phase, along with the buckling of the $CuCl_6$ octahedra. Since the organic PEA molecules support a dipole, this tilting leads to a polarization in the plane of the layers, just as the order-disorder effect in the hydrogen bond network.

1.3 (EA)CuCl Hybrid

Less information is available on a similar phase transition in the (EA)CuCl hybrid, compared to the PEA hybrid. However, the structures of both materials are very similar, except for the absence of the aromatic ring in (EA)CuCl. The phase sequence of the EA hybrid has previously been studied by (among others) visible and IR absorption spectroscopy [7, 8], birefringence measurements [9]. Above room temperature, (EA)CuCl undergoes the transition from P*bca* to C*mca* in two phase transitions at 356 K and 364 K [7]. Moreover, reference [10] claims evidence for ferroelectricity in the EA hybrid as well. Although the phase transition in (EA)CuCl has not been assessed so thouroughly as (PEA)CuCl, there is ample reason to assume far-stretching similarities between the two materials, such that the models proposed for (PEA)CuCl are also applicable on (EA)CuCl. A possible difference could be that since the ethylammonium molecule supports a significantly smaller dipole, a larger order-disorder contribution may be expected to ferroelectric properties.

2 Research goal

The phase transition in (PEA)CuCl has been studied by means of different techniques, including X-ray diffraction, birefringence measurements and Raman scattering. Two-dimensional IR spectroscopy is a technique that has been succesful at providing insight into hydrogen bond dynamics in particular. Considering the presumed role of order-disorder in the hydrogen bond network through the phase transition, these insights are interesting for the further understanding of the physics behind the phase transition and eventually for future applications.
It is expected that the NH stretching vibrations will be affected by the strength of the hydrogen bonds that are formed with chlorine atoms. Generally speaking, the stronger the hydrogen bond, the lower the frequency of the NH stretching vibration. The question is now whether the change in arrangement of the hydrogen bonds through the polar phase transition will significantly influence the hydrogen bond strengths so that they might become visible as shifts in the NH stretching frequencies. A safe prediction would be that any sign of this will be very small, considering that the phase transition concerns a change of the preferred hydrogen bond arrangement, rather than a change in bond length or strenghth.
Before embarking on complicated experiments, the preliminary work of recording static spectra of the hybrids would be useful. The goal of this thesis has been to explore experimentally the job of vibrational spectroscopy in the mid-IR frequency region (700-4000 cm^{-1}), as well as trying to find any sign of the phase transition by means of recording static temperature dependent spectra of the material.

3 Theoretical considerations

Apart from the collected data, personal insight into some essential spectroscopy physics has been one of the major side effects of producing this thesis. This section will address the theory of topics relevant for the experimental data and discussion and non-trivial on an undergraduate level.

3.1 Fourier spectroscopy - basic principles

The vast majority of data in this project was collected by Fourier Transform Infrared spectroscopy (FT-IR) using either a Total Internal Reflection (TIR) or transmission setup. Instead of using dispersive elements for measuring different wavelenghts, Fourier spectroscopy uses a setup based on the Michelson interferometer (figure 4). A parallel beam of white light is split by a half transparent mirror (beam splitter), to reflect either from a stationary mirror (M_1) or a moveable mirror (M_2), displaced by Δx. After passing the beam splitter a second time, the light focused onto the detector, where the two beams will produce interference fringes. If the sources light were monochromatic of the form $E(x,t) = E_0 cos(k_0 x - \omega_0 t)$, the field at the detector would be:

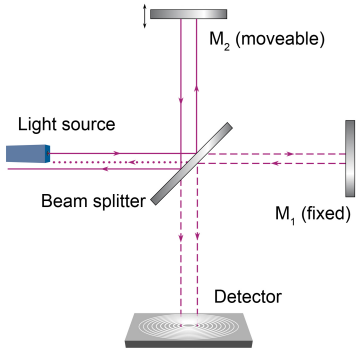

Figure 4: Michelson interferometer setup. Image adapted from Encyclopedia Britannica.

$$E_D = \frac{1}{2}\{E_0 cos(k_0 x - \omega_0 t) + E_0 cos[k_0(x + 2\Delta x) - \omega_0 t]\}. \tag{1}$$

$2\Delta x$ is the pathlength difference between the two beams. The coordinate x can be chosen 0 at the detector. By replacing $2\Delta x$ by $2x$, the electric field becomes a function of x, now the displacement of mirror M_2:

$$I(x) = c_0 \epsilon_0 \langle E^2 \rangle = \frac{c_0 \epsilon_0}{4} E_0^2 [1 + cos(2k_0 x)]. \tag{2}$$

We define the spectral intesity function $I(k) = \frac{1}{2}\int_0^\infty I(k)[1 + 2kx]\ dk$. In the monochromatic case, $I(k)$ is a Dirac-delta function. However, the relation is valid for arbitrary spectra. By rewriting we obtain:

$$I'(x) = I(x) - \frac{1}{2}\int_0^\infty I(k)\ dk = \frac{1}{2}\int_0^\infty I(k) cos(2kx)\ dk \tag{3}$$

The detector intensity as a function of path difference is therefore related to the spectral intensity over a Fourier transform. Using the Fourier transform spectroscopy has many advantages. Since the light does not have to be dispersed, the detector records the energy of the entire spectrum, improving the signal to noise ratio that is proportional to $\sqrt{E}$. Furthermore, measuring the full spectrum at the same time improves the signal at a specific wavelength, again improving the signal to noise ratio [11].

3.2 Total Internal Reflection infrared spectroscopy

An electromagnetic wave propagating from an optically dense medium (refractive index n_1 into an optically rare medium (refractive index n_2) undergoes total internal reflection if the angle

of incidence θ_i exceeds the critical angle $\theta_C = arcsin(n_{12})$, where $n_{21} = n_2/n_1$. The evanescent wave penetrating into the optically rarer medium falls off exponentially with distance normal to the boudary surface:

$$E = E_0 exp\left[-\frac{2\pi}{\lambda_1}\sqrt{sin^2\theta - n_{21}^2}z\right]$$

Here, λ_1 is the wavelength in the dense medium, λ/n_1. One can define the penetration depth d_p as the distance from the boundary where the field amplitude E has fallen off by e^{-1}. The intensity $I \propto E^2$ will be reduced with 0.25 at d_p:

$$d_p = \frac{\lambda_1}{2\pi\sqrt{sin^2\theta - n_{21}^2}}$$

The reflectivity measured is simply $R = \frac{I}{I_0} = e^{\alpha d_e}$, where d_e is the effective sampling depth, roughly $3d_p$. In practice, the effective sampling depth is dependent on the quality of the contact surface between the sample and the Internal Reflection Element (IRE), from where the light is incident.

Unlike the theoretical case of an infinite plane wave striking an infinite boudary surface, in reality, the evanescent wave does carry a net energy into the sample medium. The evanescent wave penetrating into the optically rarer medium is a non-transverse wave and can excite dipoles in all directions. The reflected light that hits the detector is called Attenuated Total Reflection (ATR) and results in an ATR-spectrum.

Internal reflection IR spectroscopy allows the sampling of solids, powders, liquids and suspensions with little to no preparation. Especially for thick or highly absorbing materials, this is a great advantage over transmission measurements [12].

Part II
Materials and Methods

4 Crystal synthesis

The samples used for all experiments were synthesized by A.O. Polyakov (RuG, Solid State Materials for Electronics), following the procedure described in ref. [1]. The crystals grow by self-assembly from a stoichiometric aqueous solution of 2-phenylethylammoniumchloride or ethylammoniumchloride and $CuCl_2$. After evaporation, the growth results in crystal platelets of a few mm^2. While the PEA hybrid crystals are brown and thick, the EA hybrid appears as fragile thin yellow sheets. The crystal's c-axis is oriented perpendicular to the platelets.

5 Experimental setup

5.1 Raman scattering

Sound crystals with few crystal domains were selected of both hybrid types. A 647 nm krypton laser was used to irradiate the materials. The Raman scattered photons were collected in a backscattering setup.
At room temperature, the Raman spectrum of both materials turned out unable to resolve individual vibrational modes in the 700-4000 cm^{-1} range. Previous recordings of the raman spectra by A. Caretta (figure 5) confirm that individual lines are poorly resolved. The best results were obtained by irradiating the sample perpendicularly to the crystal c-axis (crystal platelets mounted 'vertically' into beampath). For (PEA)CuCl a total laser output of <0.5 mW was required with long integration time to prevent burning of the sample. Since trial measurements did not yield fruitful results, the experiment was not followed up.

Figure 5: Raman spectrum (PEA)CuCl 2900-3200 cm^{-1}

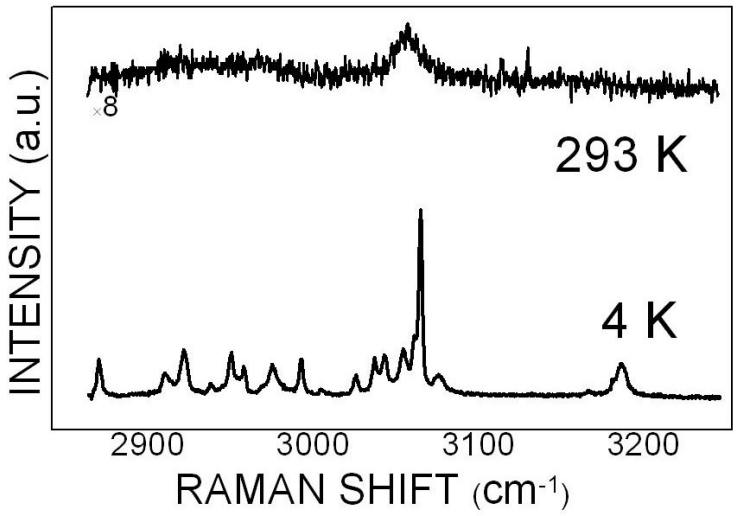

Measurement by A. Caretta (RuG, Optical Condensed Matter Physics).

5.2 TIR infrared spectroscopy

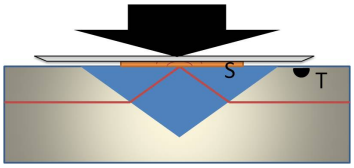

Figure 6: ATR setup. S: sample, T: temperature sensor.

Recordings of temperature dependent spectra of both (PEA)$CuCl_4$ and (EA)$CuCl_4$ were done using a Bruker IFS88 FT-IR spectrometer, equiped with a single 45° reflection Specac Golden Gate diamond internal reflection element (IRE). Unprepared samples were pressed into optical contact between the IRE and a razor blade by applying a clamping torque of 0.8 Nm.
Three temperature dependent measurement series were recorded for (PEA)CuCl and two for (EA)CuCl under different experimental conditions:

1. (PEA)CuCl in a temperature range rising from 295 - 410 K. The resolution used was 4 cm^{-1} and the spectra were calculated after averaging over 100 reflections;

2. (PEA)CuCl and (EA)CuCl in a temperature range rising from 303 K - 373 K and falling temperature to 340 K. For (PEA)CuCl, a few additional spectra were recorded at rising temperatures to confirm the consistency of the measurements. Resolution: 2 cm^{-1}, reflections per spectrum: 240.
   During these measurements, the sample was kept in an N_2 flooded environment in order to reduce the spectral features of H_2O and CO_2.

3. (PEA)CuCl and (EA)CuCl ATR spectra were recorded in the same setup as series 2. The measurements at different temperatures were done in alternating order: 360 K, 310 K, 355 K, 315 K etc. A time of 12 minutes for temperature stabilisation between consecutive measurements was taken into account.

5.3 Infrared transmission

A transmission setup was built as shown in figure 7. BaF_2 windows and a thin film sample of the hybrids on a BaF_2 substrate were used to provide optimal IR transmission, BaF_2 having a transparancy region from 870 to 40000 cm^{-1}. For the samples, readily sythesized (PEA)CuCl and (EA)CuCl crystals were dissolved into a saturated ethanol solution at 50°C. At room temperature, the solution was applied onto the substrate where cloudy yellow films were formed after evaporation of the solvent. Three measurement series were recorded, all with a 2 cm^{-1} resolution and 240 reflections per spectrum. In all cases, the measurement of the background absorption was done prior to evacuating the cryostat, accounting for a slight overcorrection of atmospheric spectral lines.

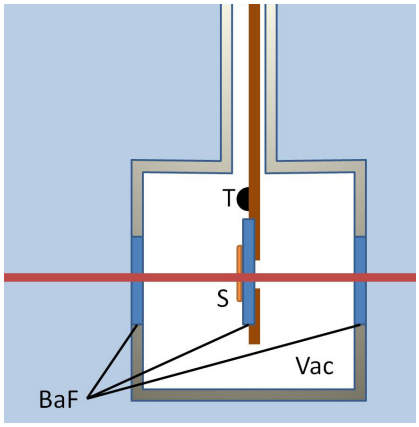

Figure 7: Setup of the transmission experiment. BaF: Barium fluoride windows and substrate, S: sample, Vac: evacuated cryostat, T: temperature sensor.

1. (PEA)CuCl in a temperature range falling from 355 K to 320 K;

2. (PEA)CuCl in a temperature range rising from 130 K to 296 K;

3. (EA)CuCl in a temperature range rising from 80 K to 296 K.

Part III
Experimental results

6 Assignment of bands to their corresponding modes

6.1 (EA)CuCl

Figures 8 and 9 show the infrared spectra recorded at room temperature by ATR-IR spectroscopy of both (PEA)CuC and (EA)CuCl. In order to know what there is to see, the spectral bands were assigned to their corresponding modes by comparison with a study done by Rao e.a. on (among others) (EA)CdCl and (EA)MnCl.

(EA)CuCl [7]	**(EA)CdCl [13]**		**(EA)MnCl [13]**			**(EA)CuCl**
295 K	298 K	173 K	303 K	173 K	Assignment [13]	298 K (Current)
3300-3450	3140[a]	3140[a]	3130	3130	asym. ν NH_3	3149sh[b]
	3120[a]	3120[a]				
		3100				
3040-3050	–	3040s	3050s	3050s	sym. ν NH_3	3096s[b]
2900-3040	2950s	2950s	2950sh	2955sh	asym. ν CH_3	2950s
	–	2912sh	2920 sh	2920m	asym. ν CH_2	
	2880sh	2880m	2880sh	2890m	sym. ν CH_3	
2700	2820sh	2820m	–	2820m	sym. ν CH_2	
	–	1914sh	–	1952sh	asym. δ NH_3 + τ CN	
		1905s		1892s		
				1850sh		
	–	–	–	1750w	asym. δ CH_3 + τ CN	
1600	1605s	1606m	1575s[b]	1688m	asym. δ NH_3	1569s
		1590s		1583s		
	1485m	1494s	1485s	1500s	sym. δ NH_3	1485s
	1475s	1479s	1472sh	1478m	δ CH_2	
		1467w				
1450	1450sh	1455m	1454sh	1454w	asym δ CH_3	
	1403m	1408	1405m	1405m	sym δ CH_3	1397m
	–	1375w	1375w	1375m	ω CH_2	
1200	1215	1220	1210	1215	ρ CH_3	1185s
1050			1185s			
	1042s	1040s	1045m	1043m	ν CN	1048s
970	965s	980s	966s	975s	ρ NH_3	965s
		973s		968s		
	868m	870m	872m	872m	ν CC	872w
	790s[b]	795s	791s	795m	ρ CH_2	788s

Table 1: Vibrational frequencies of (EA)CuCl and their assignment, compared to previous experimental studies of similar structures by Kapustianyk et al. [7] and Rao et al [13]. The appearance of absorption lines is qualifies as strong (s), medium (m), weak (w) or shoulder type (sh). ν stretching mode; δ deformation mode; τ torsional mode; ρ rocking mode.

Figure 8: ATR spectra of (PEA)CUCl and (EA)CuCl at room temperature

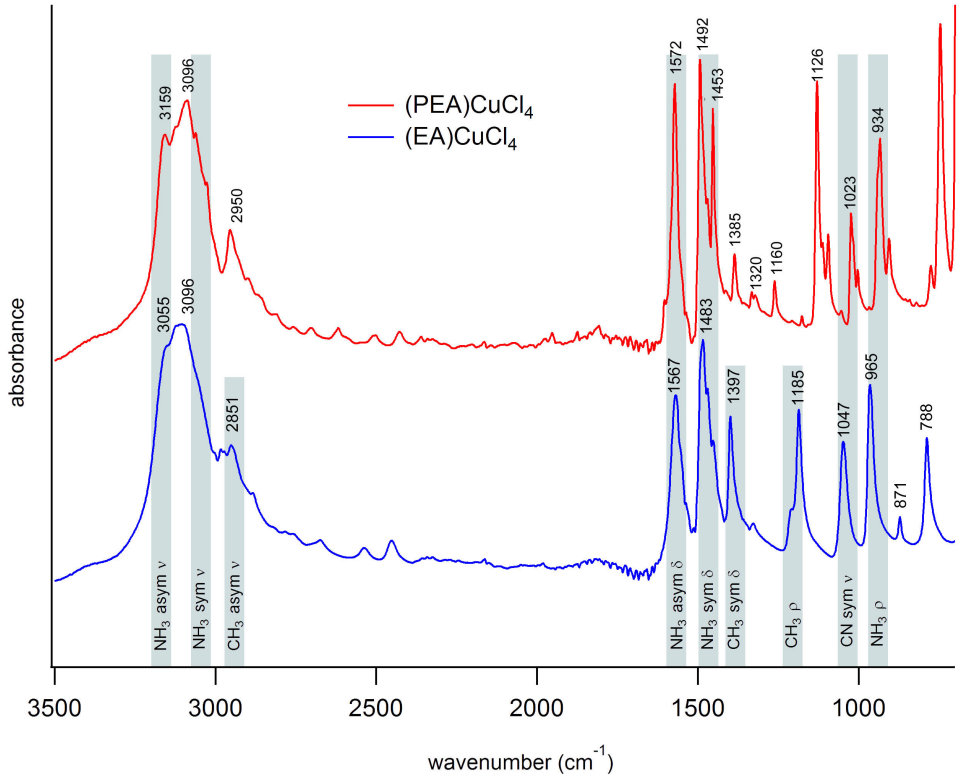

Comparison of the ATR-IR spectra of (PEA)CuCl and (EA)CuCl. Grey bands of width ± 30 cm^{-1} are plotted at the frequencies found in references [7, 13] for (EA)CuCl and, (EA)CdCl and (EA)MnCl. Local maxima in both spectra are labeled with their wavenumber.

Beside this specific assignment of modes, it is known that the NH vibrations can be found at wavenumbers 3000-3500 (stretching modes) and 1400-1600 (bending modes). Therefore, these spectral regions are of special interest. Since the (EA)$CuCl_4$ contains the same organic molecule as used by Rao e.a., the absorption lines were assigned analogously to the corresponding vibrations.

6.2 (PEA)CuCl

For the (PEA)CuCl crystal, the spectrum is richer and more complicated due to the presence of vibrations of the aromatic ring. For deciphering the (PEA)CuCl spectrum, comparison with liquid ethylbenzene has also proven itself useful. Table 1 shows the assignment of vibrational modes as done by ref. [13]. Identifying the vibrations associated with the absorption lines has therefore been much more cumbersome and the final result will not be flawless. A comparison with the spectrum of liquid ethylbenzene allows for the identification of bands that belong to either aromatic C-H stretcing or N-H stretching modes. Beside that, calculations by R.W. Havenith were used in order to provide insight into the distribution of vibrations over the measured spectral range.

Figure 9: ATR spectra of (PEA)CuCl and liquid Ethylbenzene

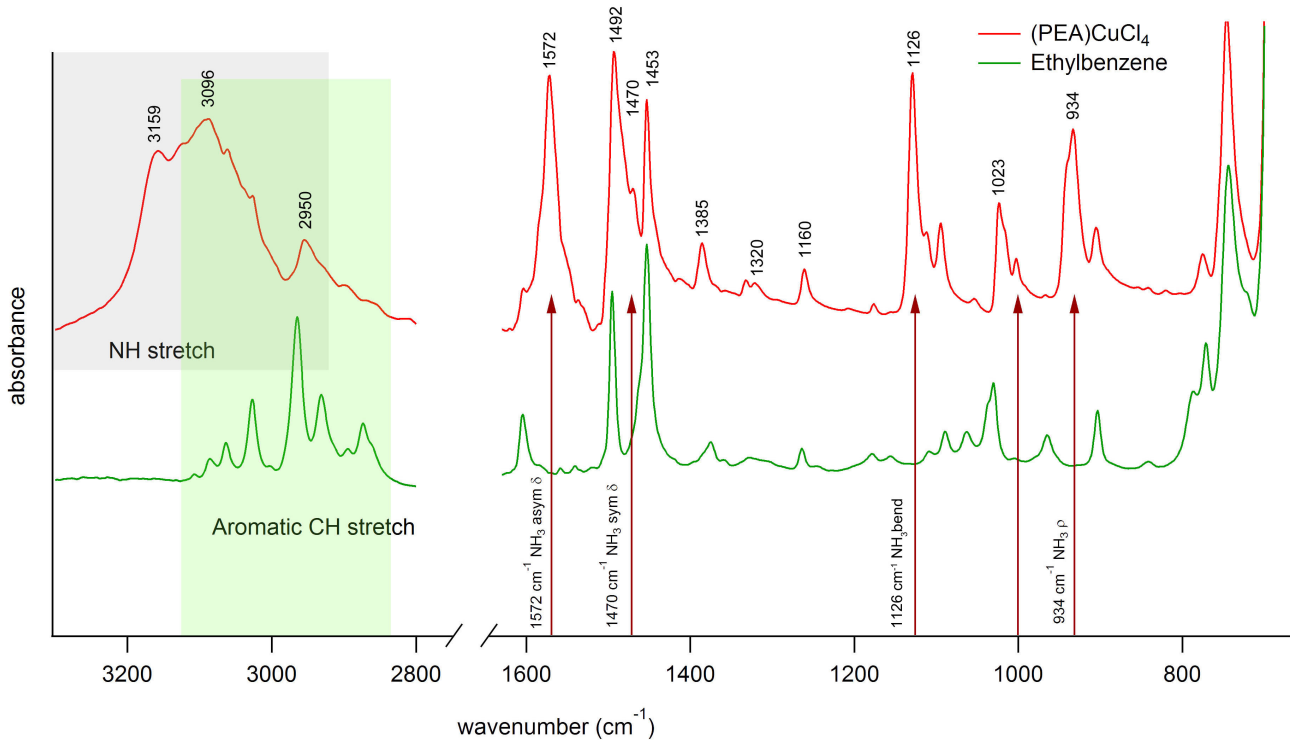

Comparison of the ATR-IR spectra of (PEA)CuCl (red) and liquid ethylbenzene (green). Green shaded: frequency region of (aromatic) CH stretching vibrations. Grey shaded: frequency region of NH stretching vibrations. The lines that are unique to (PEA)CuCl are assigned as vibrations of the NH_3 group. Local maxima in the (PEA)CuCl spectrum are labeled with their wavenumber.

Calculated vibration frequencies

For the (PEA)CuCl, the frequencies of vibrational modes were calculated by Remco Havenith (RuG, Theoretical Chemistry Group). This resulted in a total of 564 vibrational modes, ranging from 0 to 3136.3 cm^{-1}. The relative motions of the atoms were classified as a stretching type, bending type, a (probably) rotational type and 'other' modes. The distinction was made based on the contribution of three components to the movement of atom A relative to atom B: along the A-B line, in plane of a specified tird atom C and an out of plane motion. From the 564 calculated modes, 73 involve a motion of a H atom relative to an N atom. In figure 10, the frequencies of the calculated NH modes are plotted as lines against the experimental (PEA)CuCl spectrum recorded by ATR. From the graph it becomes clear which strong absorption lines in the 700-1600 cm^{-1} coincide with a high density of NH vibrational modes. In the 2900-3200cm^{-1} range of the spectrum, the NH modes are more equally spread and alternated by aromatic CH stretching modes, probably explaining for the broad band and less distinguishible lines.

Figure 10: (PEA)CuCl spectrum and calculated NH_3 vibration frequencies

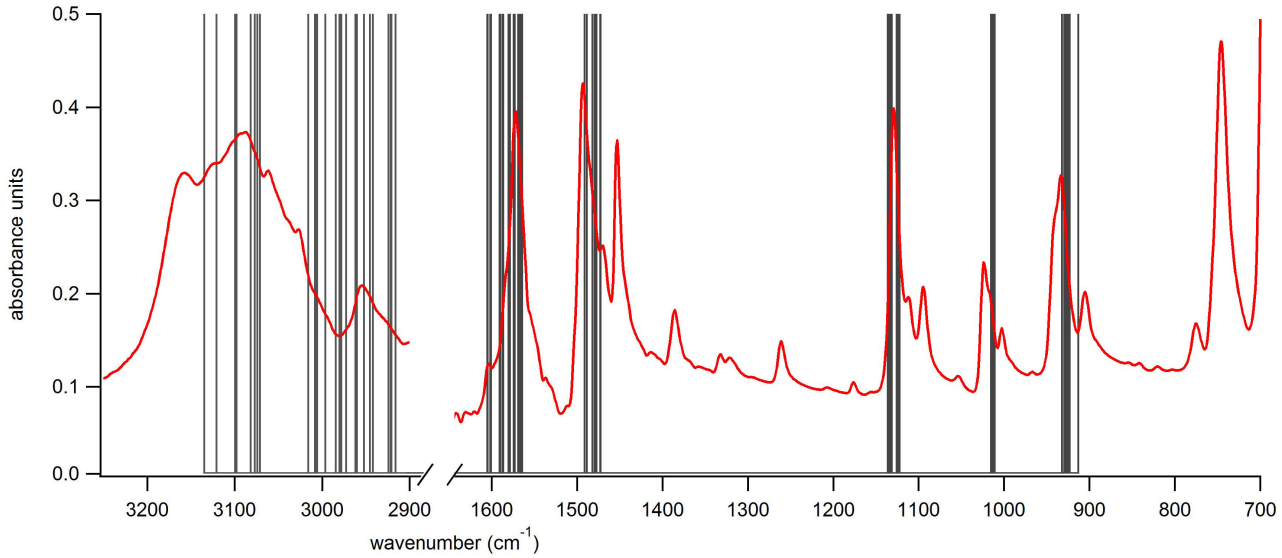

Red: ATR-IR spectrum of (PEA)CuCl at room temperature. Grey: frequencies of calculated NH vibrations, no amplitude.

In figure 10 only the 73 calculated vibrations from a total of 564 are displayed. The ranges of the NH_3 bending en stretching modes are much overlapped by aromatic ring bending and (aromatic) CH stretching modes. Based on the comparison with the ethylbenzene spectrum, the 2950 cm^{-1}, 1492^{-1} and 1453^{-1} lines have been assigned to CH stretching and two aromatic ring bending modes respectively [14]. Subsequently, the NH_3 absorption lines in the experiment were assigned as follows:

Mode	**Calculated frequency**	**Assigned to line (296 K)**
asym. ν NH_3	3072 - 3136	3159[a]
(aromatic) ν CH	2915 - 3097	2950
sym. ν NH_3	2917 - 3017	3096[a]
asym. δ NH_3	1565 - 1606	1572
aromatic CC δ	1494 - 1534	1492
sym. δ NH_3	1473 - 1492	1470
aromatic CC δ	1452 - 1472	1453
bending (?) NH_3	1124 - 1138	1126
ν CN	1012 - 1016	1002
ρ CH_3	914 - 933	934

Table 2: [a] Part of a broad intense band

7 Temperature dependent static IR spectra

For all plots in this and the following sections, the absorbance units (or: optical density) A_{10} are specified by Bruker as: $A_{10} = -log(I_R/I_0)$. Here, I_R is the reflected intensity and I_0 the incident intensity. The absorbance peak intensities are corected for the temperature changes in the average absorbance over a lower frequency range (900 - 1600 cm^{-1}) and a higher frequency range (2500-3200 cm^{-1}. These data are presented in figure 14.

7.1 313-400 K ATR-IR spectra of (PEA)CuCl

Figure 11 to 13 show the temperature dependence of the optical density, measured in the three different measurement series described in the experimental methods section. The plotted lines are assigned to:

3159 cm^{-1}: asymmetrical NH_3 stretching;
3096 cm^{-1}: symmetrical NH_3 stretching;
1572 cm^{-1}: asymmetrical NH_3 deformation;
934 cm^{-1}: NH_3 rocking;

2950 cm^{-1}: (aromatic) CH stretching;
1492 cm^{-1}: aromatic ring bending;
1453 cm^{-1}: aromatic ring bending;
1126 cm^{-1}: NH_3 bending;

Figure 11: (PEA)CuCl: Temperature dependence of absorption line intensity. Measurement series 1

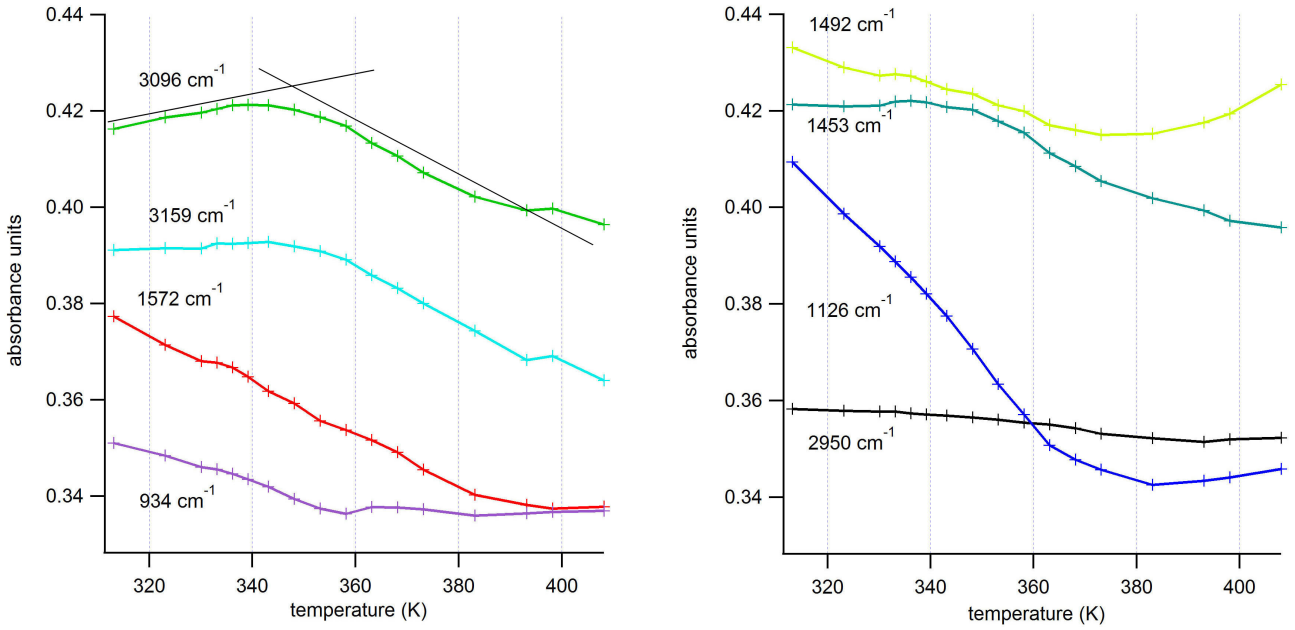

The 'bending' accentuated in the 3096 cm^{-1} line of these and following plots is summarized in table 3.

Figure 12: (PEA)CuCl: Temperature dependence of absorption line intensity. Measurement series 2

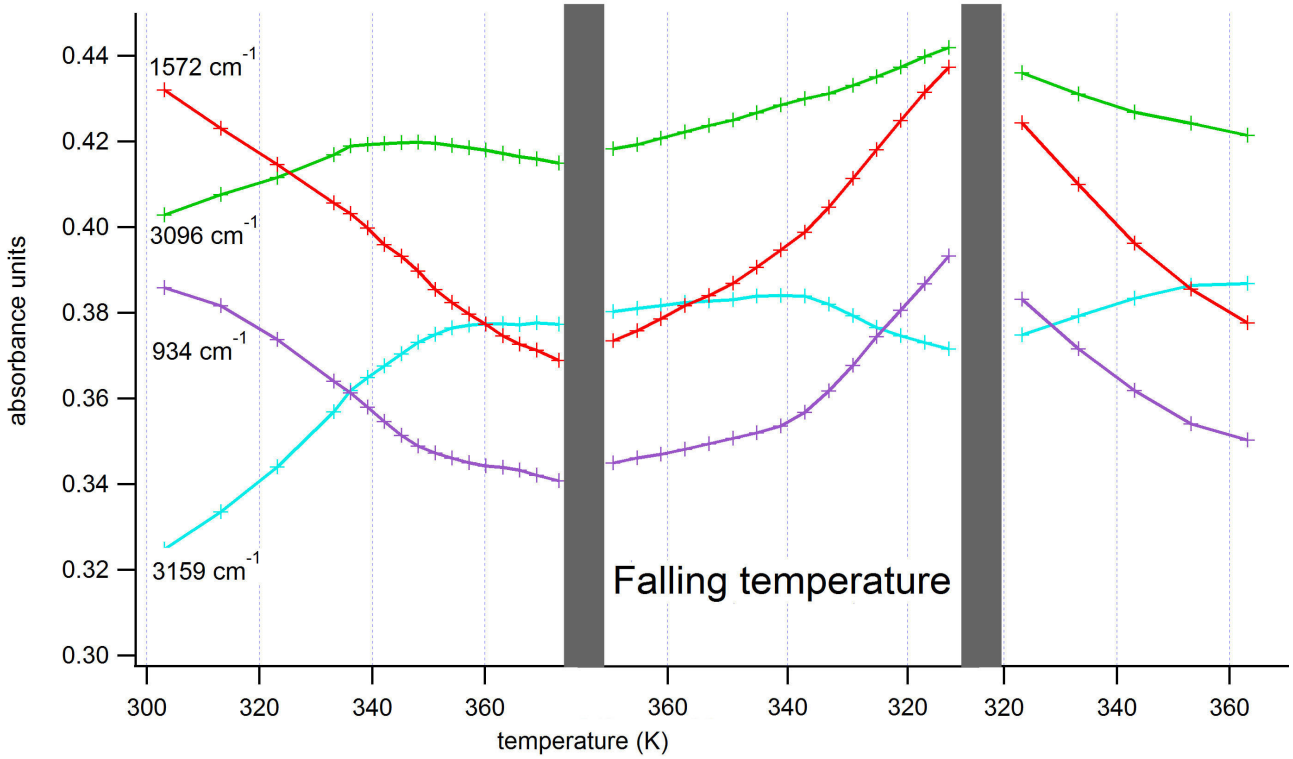

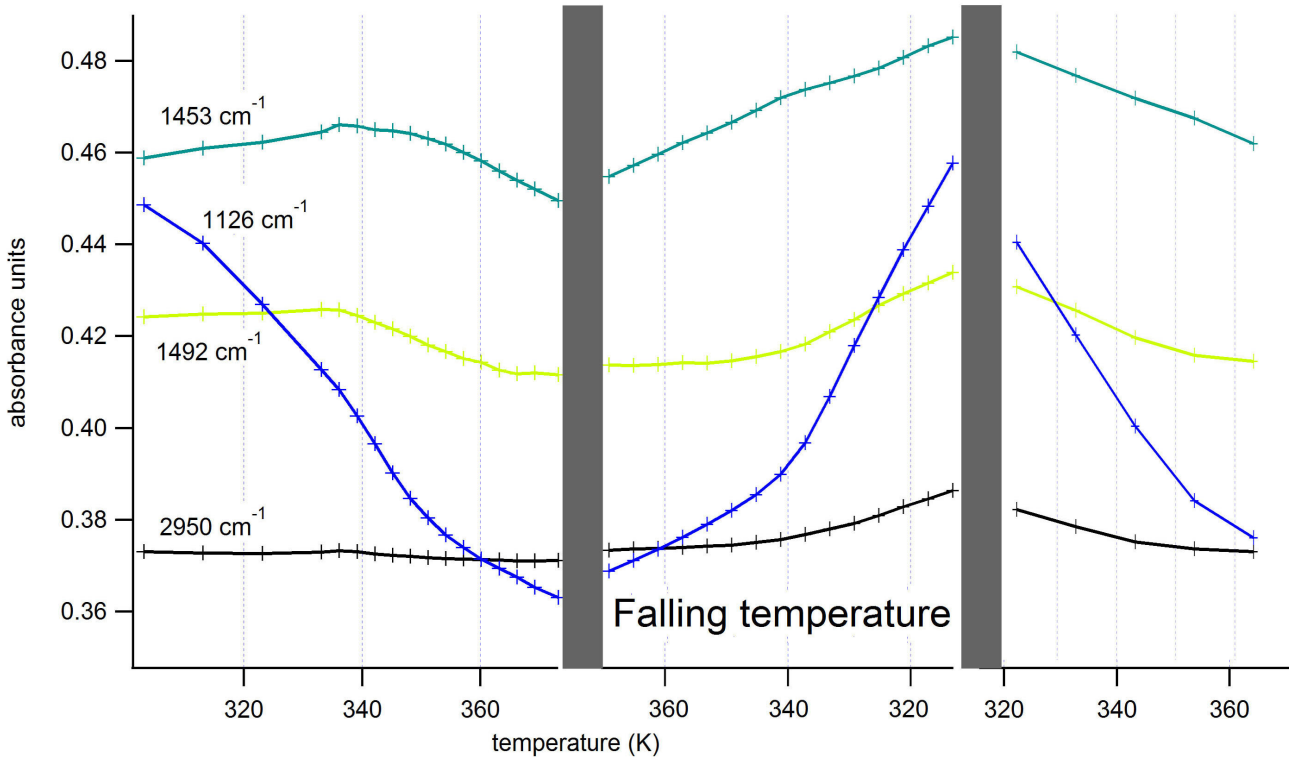

Figure 13: (PEA)CuCl: Temperature dependence of absorption line intensity. Measurement series 3

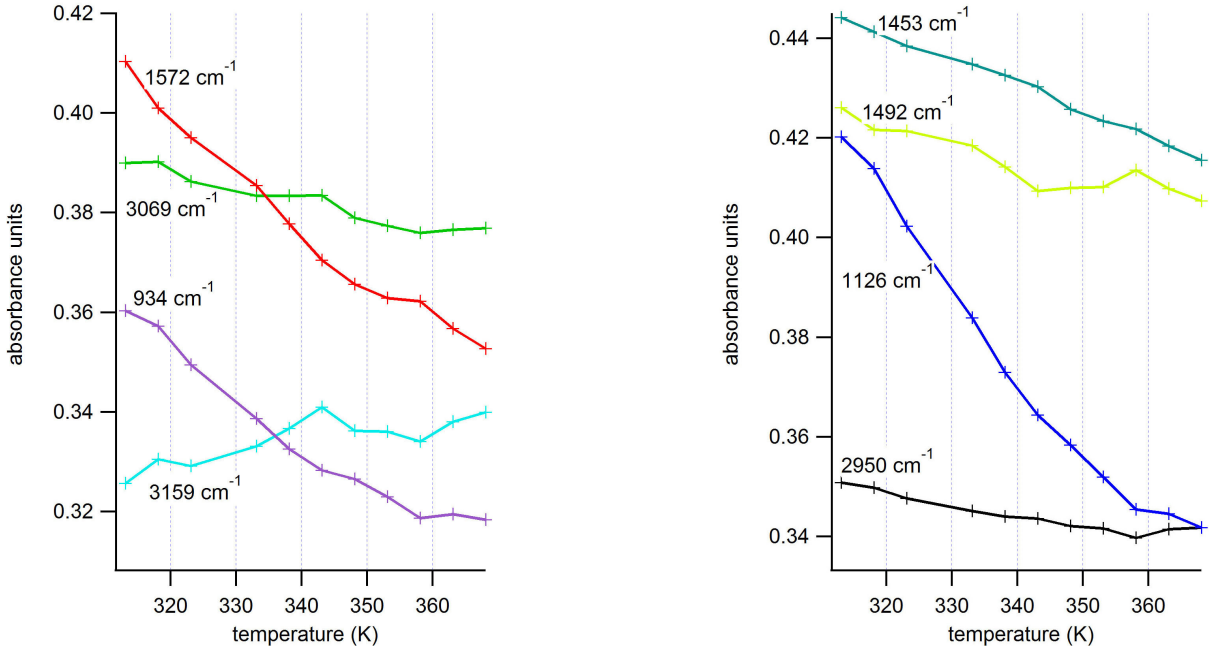

Figure 14: (PEA)CUCl: Temperature dependence of average absorbance 900-1600 cm^{-1} and 2500-3200 cm^{-1} .

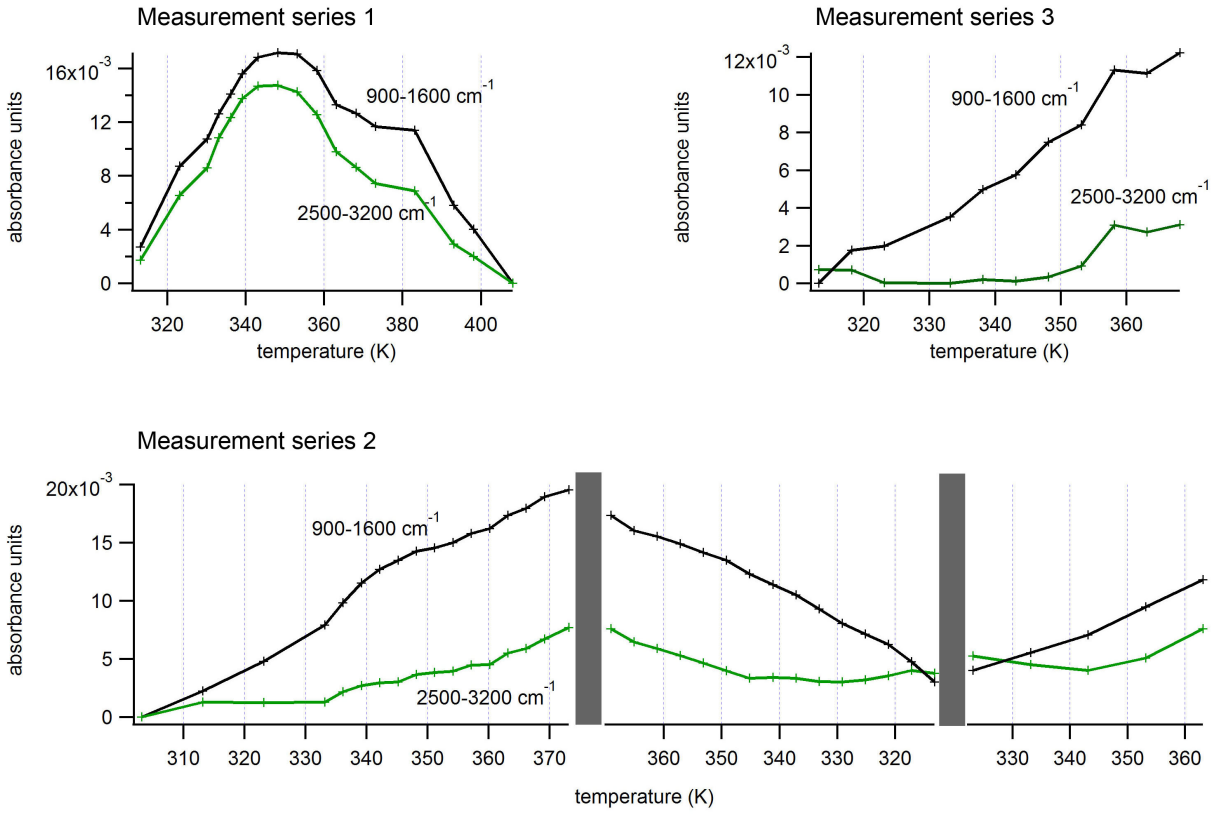

Line (cm^{-1})	Series 1			Series 2, rising T			Series 2, falling T		
	$\frac{dA_{10}}{dT}\|_{T<T_b}$	$\frac{dA_{10}}{dT}\|_{T>T_b}$	T_b	$\frac{dA_{10}}{dT}\|_{T<T_b}$	$\frac{dA_{10}}{dT}\|_{T>T_b}$	T_b	$\frac{dA_{10}}{dT}\|_{T<T_b}$	$\frac{dA_{10}}{dT}\|_{T>T_b}$	T_b
3159	0.4 ± 0.2	-5.0 ± 0.2	348	11.0 ± 0.3	0.9 ± 0.3	340	5.3 ± 0.3	-1.2 ± 0.1	337
3096	1.7 ± 0.2	-4.2 ± 0.2	343	4.7 ± 0.2	-1.4 ± 0.2	351	-4.2 ± 0.1	—	—
1572	-5.3 ± 0.1	—	—	-9.5 ± 0.2	—	—	-16.3 ± 0.2	-7.8 ± 0.3	337
934	-3.4 ± 0.1	-0.1 ± 0.1	355	-8.6 ± 0.4	-3.0 ± 0.2	348	-15.4 ± 0.2	-3.4 ± 0.2	337
2950	-0.8 ± 0.1	—	—	-0.4 ± 0.1	—	—	-3.9 ± 0.2	0.8 ± 0.1	340
1492	-3.0 ± 0.1	2.9 ±0.7	373	0.5 ± 0.1	-4.8 ± 0.1	336	-0.7 ± 0.1	—	—
1453	-0.1 ± 0.2	-4.2 ± 0.3	348	2.0 ± 0.2	-4.9 ± 0.3	340	-6.1 ± 0.2	-5.3 ± 0.1	340
1126	-11.4 ± 0.3	0.2 ± 0.6	373	-14.7 ± 0.7	-7.7 ± 0.4	351	-25.0 ± 0.4	-7.4 ± 0.3	340

Table 3: The change in slope of the absorbance-temperature plots is represented in this table by the slopes of two linear fits below and above the bending temperature (if present).

Discussion

Temperature induced changes in the spectrum are shown to be small. They are of the same order of magnitude as observed discrepancies caused by using different crystals, IRE-sample contact quality, detector stability (temperature). Still, two features of the measurements are noteworthy.

As can be seen from figure 15, the high frequency part of the broad band containing the absorption lines of the CH and NH stretching modes becomes more intense with rising temperature, whereas overall absorbance decreases. The latter makes sense considering the Maxwell-Boltzmann distribution of vibrational states. The shift from decreasing to increasing absorbance above 3090 cm^{-1} may be interpreted as a blue-shifting of an underlying structure.

Figure 15: (PEA)CuCl spectrum 3000-3200 cm^{-1}.

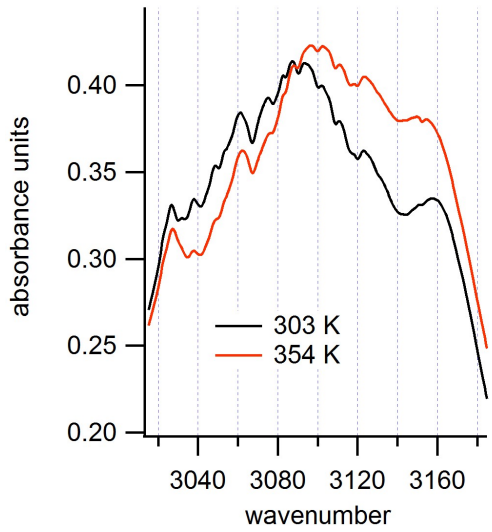

Along with this, many of the lines plotted in figures 11-13 show an apparent bend, occurring in a temperature range from 335-350 K. The changes in dA_{10}/dT are quantified in table 3, for which the direction of the curves was fitted with straight lines below and above the bending temperature. Measurement series 3 was excluded from the table, since the bending of the curves did not become visible, perhaps because of the non-gradual variation of the temperature. In the high temperature region, the bending could agree with the blue shifting of something underneath.

7.2 313-373 K ATR-IR spectra of (EA)CuCl

Figure 16 to 18 show the temperature dependence of (EA)CuCl absorption lines in two measurement series as described in the experimental methods section: rising/falling temperature in range 313 - 373 K and alternating temperatures in range 313 - 373 K. The plotted lines are:

3155 cm^{-1}: asymmetrical NH_3 stretching;
3096 cm^{-1}: symmetrical NH_3 stretching;
1567 cm^{-1}: asymmetrical NH_3 deformation;
1483 cm^{-1}: asymmetrical NH_3 deformation;
965 cm^{-1}: NH_3 rocking;
2950 cm^{-1}: CH stretching;
1397 cm^{-1}: symmetrical CH_3 deformation;
1185 cm^{-1}: CH_3 rocking;

Figure 16: (EA)CuCl: Temperature dependence of absorption line intensity. Measurement series 2

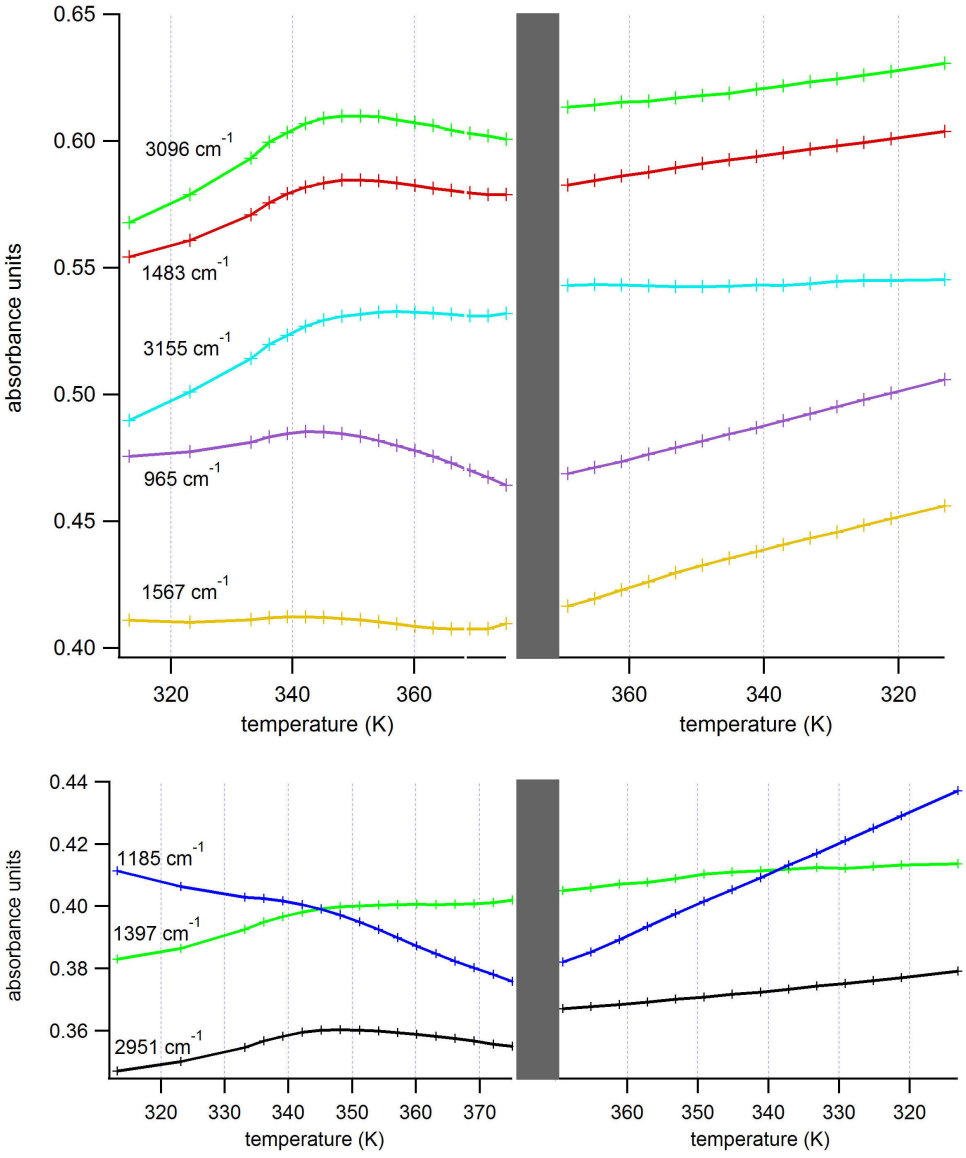

Figure 17: (EA)CuCl: Temperature dependence of absorption line intensity. Measurement series 3

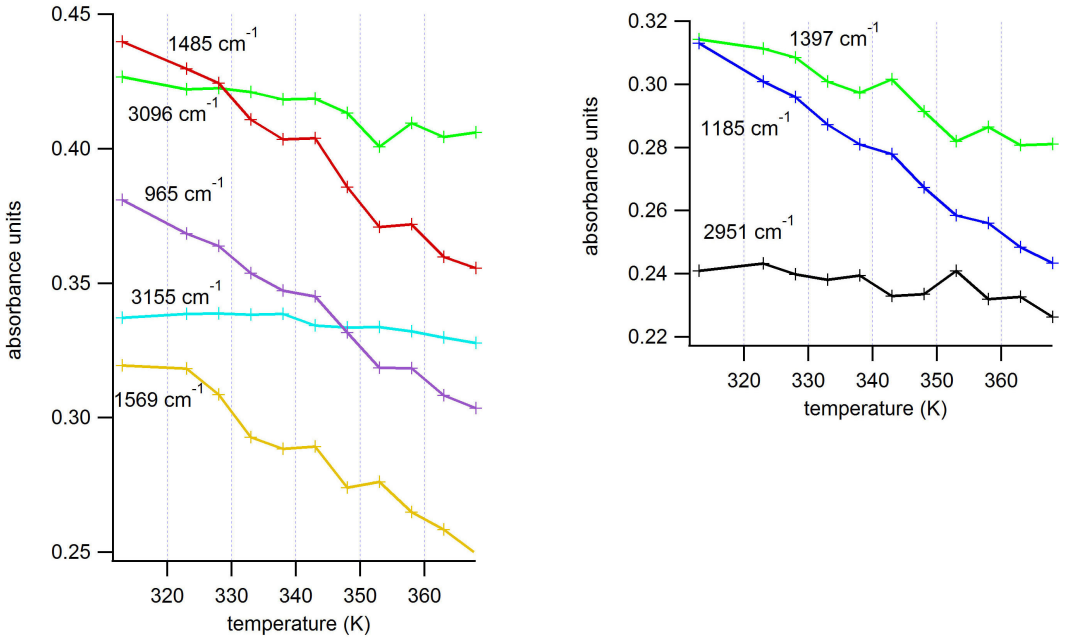

Figure 18: (EA)CUCl: Temperature dependence of average absorbance 900-1600 cm^{-1} and 2500-3200 cm^{-1} .

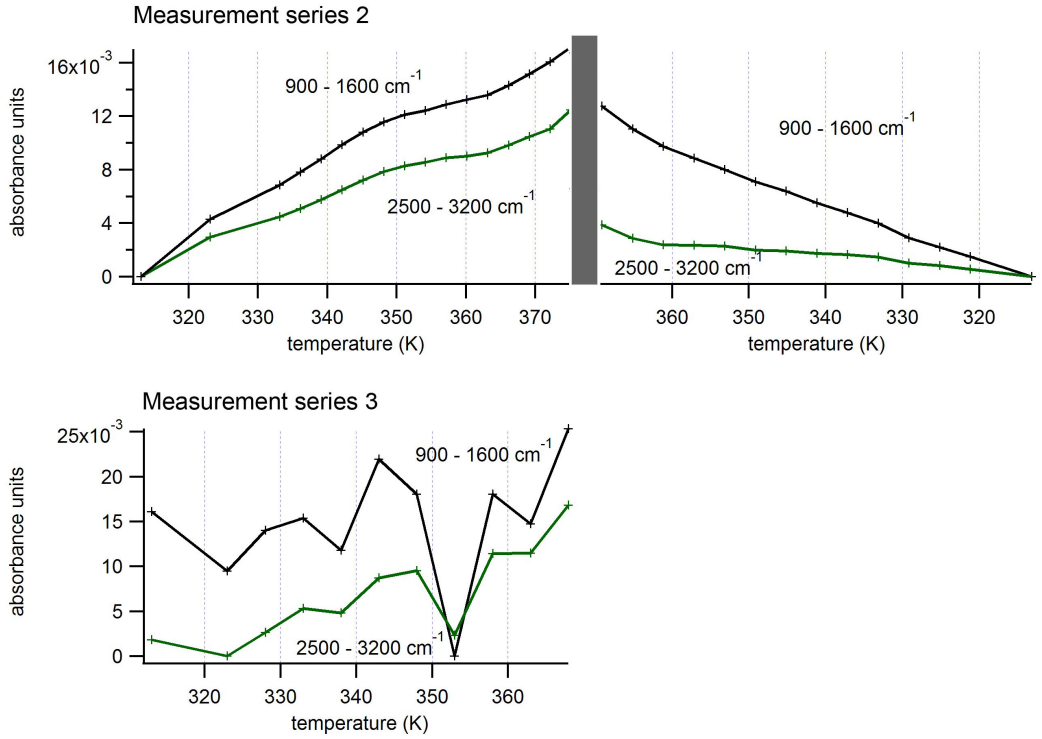

Discussion

A similar two-step phase transition is expected at temperatures of 356 K and 364 K. In contrast to (PEA)CuCl, the (EA)CuCl data show little to no consistency, even in a single measurement series. Although a similar bending of absorbance-temperature graphs occurs in at about the same temperature as (PEA)CuCl in rising temperature, no symmetry is observed in falling temperature series.
The lack of consistency in the data suggests that temperature adjustments affect the (EA)CuCl hybrid in a different way than the (PEA)CuCl hybrid or that there are other parameters influencing the absorbance of the material during the experiment. It allows no other conclusion than that in this case, the experiment is inadequate.

7.3 313-356 K Transmission IR spectra of (PEA)CuCl

In transmission, the spectrum differs in some aspects from the ATR spectrum. These differences along with their interpretation are discussed in section 8. Clear absorption maxima were found at frequencies:

Transmission line (cm^{-1})	ATR line (cm^{-1})	Assignment
3166	3159[a]	NH stretching
3126	3096[a]	NH stretching
1572	1572	asymmetrical NH_3 deformation
1453	1453	aromatic ring bending
1129	1126	NH_3 bending
930	934	NH_3 rocking

Table 4: [a] No exact correspondence of lines.

Figure 19: Temperature dependence of absorption line intensity.

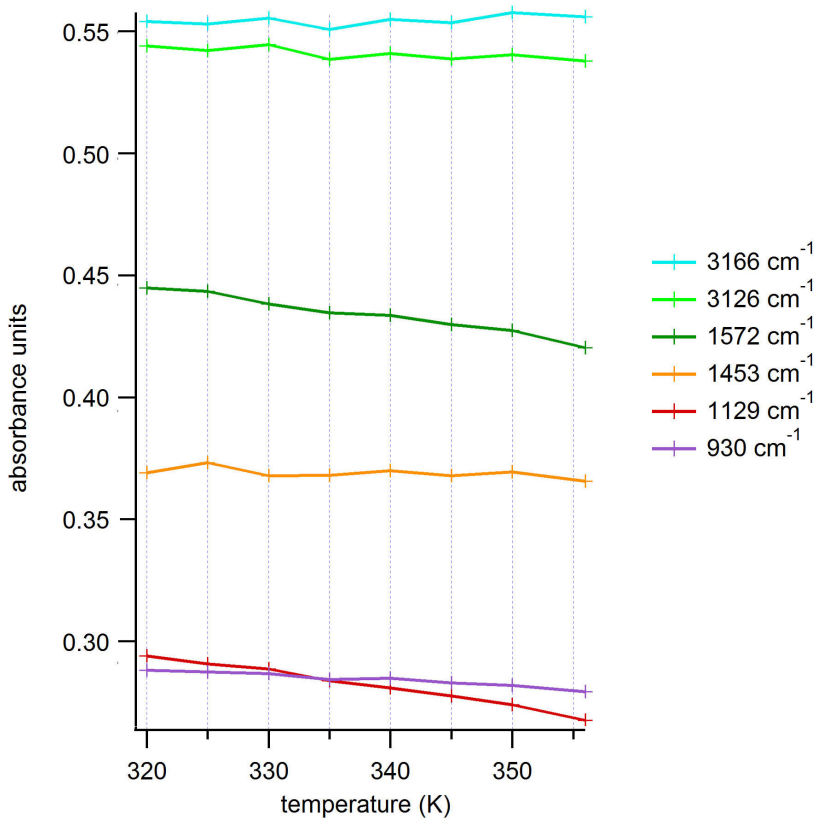

Discussion

Except for a minute softening of most of the absorption lines, none of the features seen in the temperature dependent ATR-spectra recur in the transmission spectra in the same temperature range.

7.4 Low temperature transmission spectra

Figure 20: (PEA)CuCl transmission spectra 2900-3250 cm^{-1} from 130-296 K

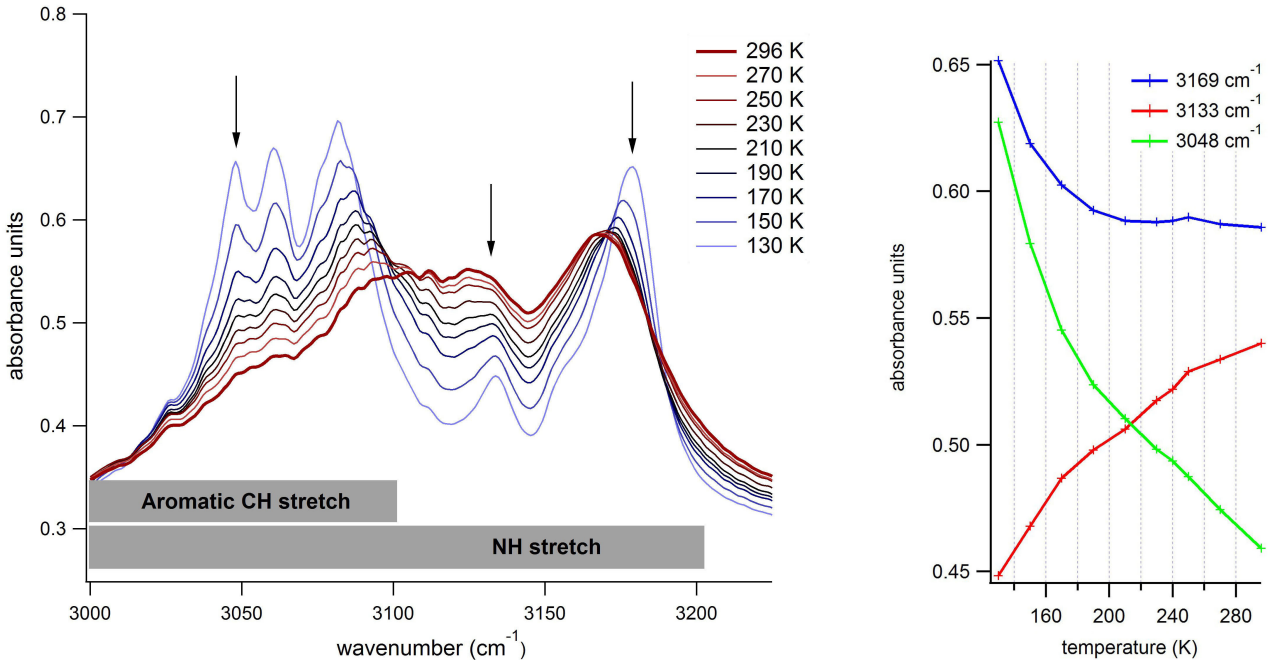

3169 cm^{-1} Peak undergoes a redshift of 8 cm^{-1}.

Figure 21: (EA)CuCl transmission spectra 2900-3250 cm^{-1} from 80-296 K

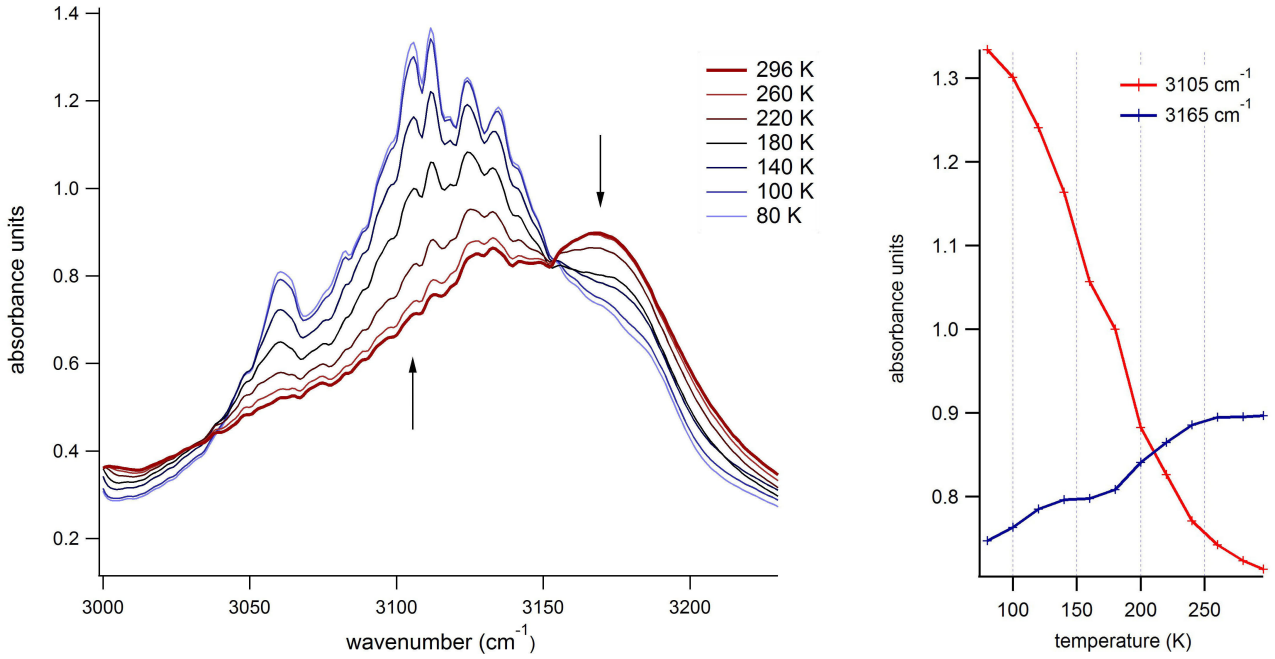

Figure 22: (PEA)CuCl transmission spectra 900-1600 cm^{-1} from 130-296 K

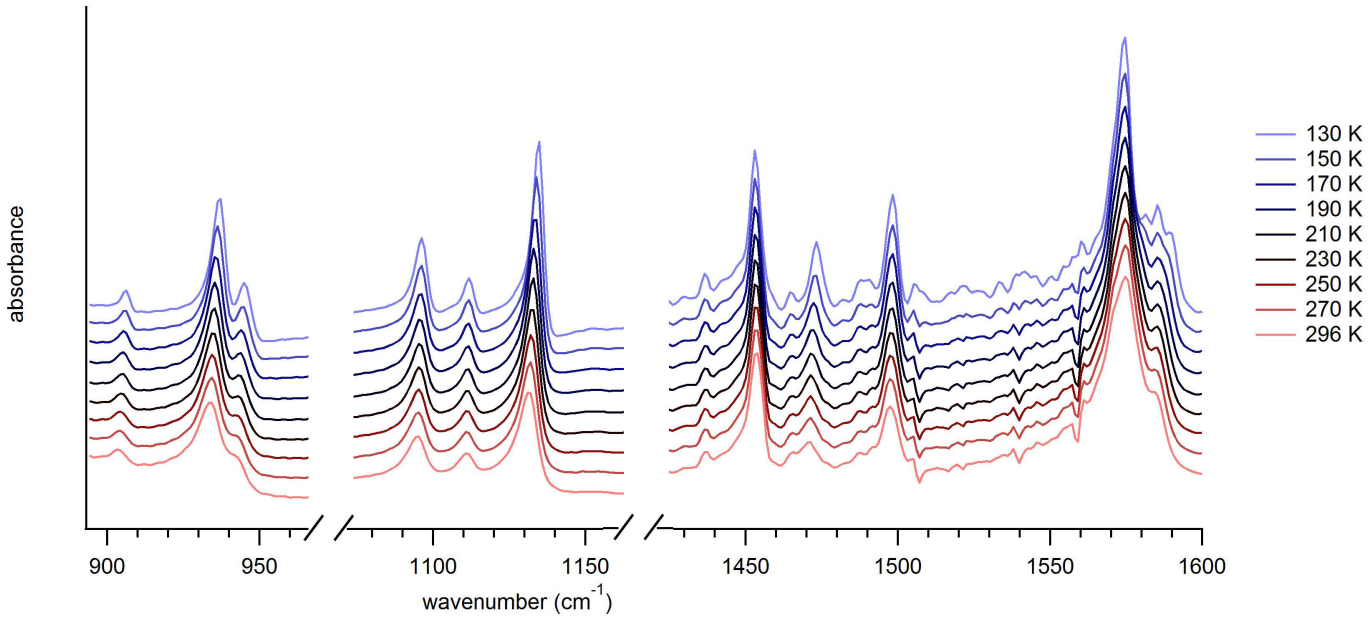

Figure 23: (EA)CuCl transmission spectra 900-1600 cm^{-1} from 130-296 K

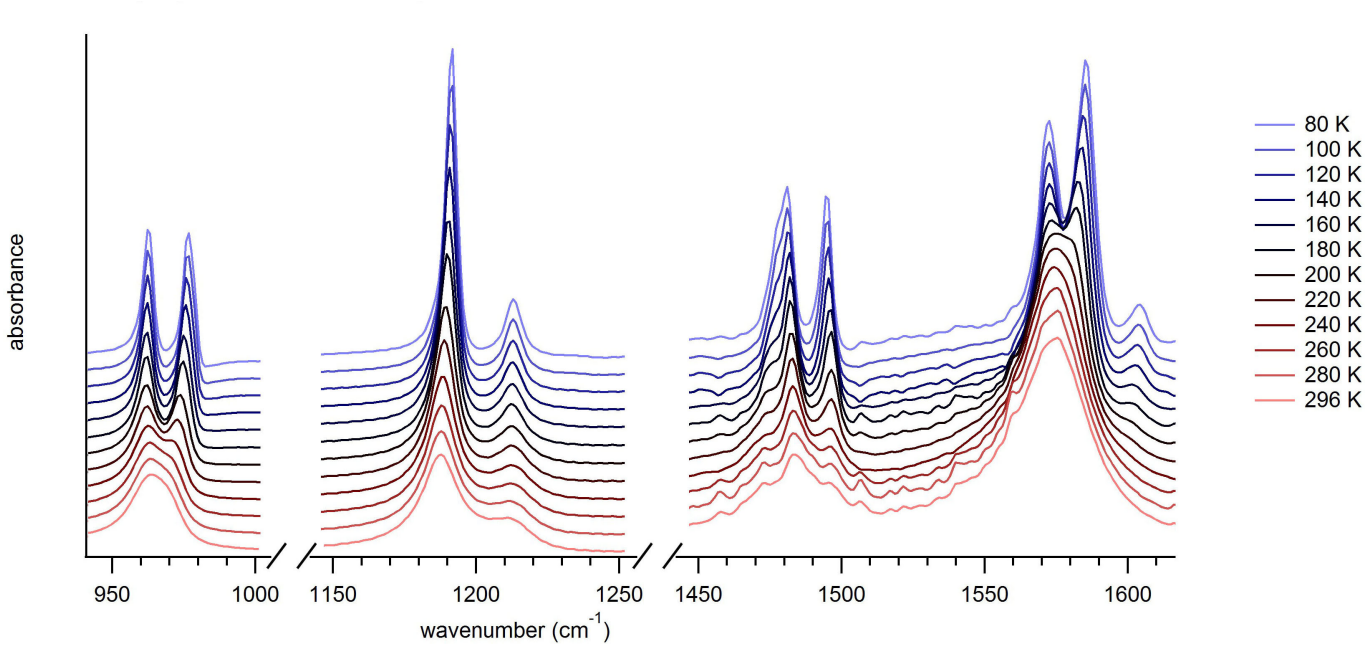

Discussion

Low temperature spectra of (PEA)CuCl and (EA)CuCl were recorded to acquire an improved resolution of the individual lines that make up the broad 2900-3200 cm^{-1} absorption band. In contrast to the expectation, the (EA)CuCl appears to be just as complex as the (PEA)CuCl

spectrum in ths frequency region, despite the absence of all aromatic vibrations.
In the 900-1600 cm^{-1} range, the (PEA)CuCl spectrum shows only a slight softening of lines with increasing temperature, whereas in the (EA)CuCl spectrum, lines shift, merge and almost vanish in the same temperature range.

Figure 24 displays the the spectra of the second ATR measurement series and the low temperature transmission of (PEA)CuCl, from which the specta at 303 K and 130 K were substracted respectively. A decrease of the spectrum in the 3010-3090 cm^{-1} interval and the simultaneaous rising in the 3090-3200 cm^{-1} interval was mentioned before as a possible sign of a blue shifting structure. From the difference graphs it can be seen that this feature sets in at a temperature below 130 K. The rise in absorbance in the 3010-3090 cm^{-1} is partly to be attributed to the broadening of the bands below 3090 cm^{-1}. However, under the assumption that lines broaden symmetrically with temperature, one would expect a comparable rise of the spectrum in the 2900-3060 cm^{-1} interval of the spectrum. Since this is much less the case, a blue shifting structure remains a possible interpretation for the falling-rising correlation.

Figure 24: (PEA)CuCl difference spectra

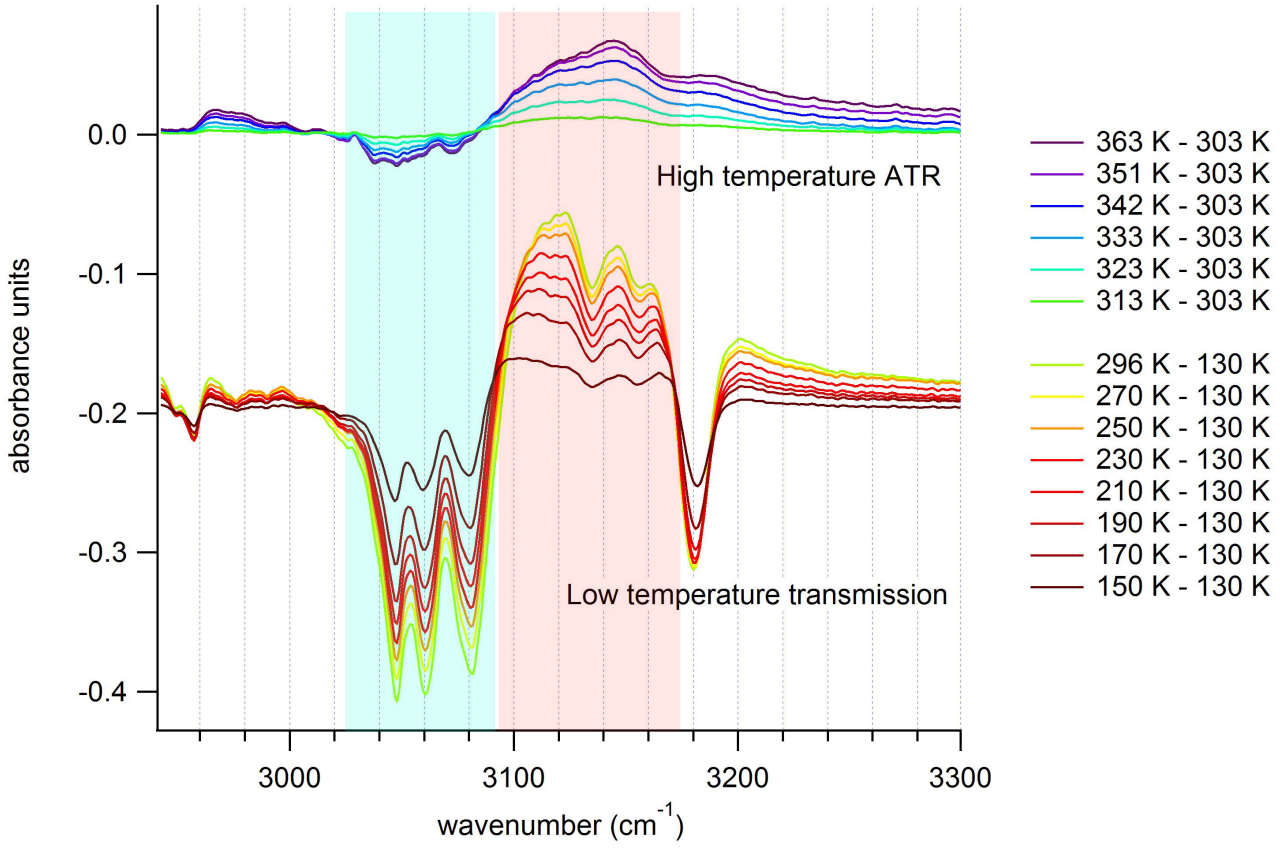

Above: ATR spectra of (PEA)CuCl (313-363 K, measurement series 2) after subtraction of the 303 K spectrum. Below: transmission spectra of (PEA)CuCl (150-296 K) after subtraction of the 130 K spectrum. The difference spectra of the transmission experiment are plotted with a -0.2 vertical offset.

Part IV

8 Discussion

8.1 Experimental conditions

Among other things, the sample quality, applied pressure in TIR, detector temperature and atmospheric spectral lines are factors that account for errors in the same order of magnitude as temperature effects. Controlling these parameters has been attempted as much as possible, however nothing can be said conclusively to what extent the influence of these paramenters has been reduced. At this stage, the small changes with temperature in especially the ATR spectra can not be considered as significant information.

8.2 Sample quality

TIR

Total internal reflection measurements required no further preparation of the crystals before sampling, but the measurement setup does not allow for subtle treatment of the samples. Under high pressure (80 Ncm clamping torque), the samples were pulverized during measurements. Although a less violent pressure did result in qualitatively acceptable spectrum, the signal strength would become less stable. Heating the sample through the ATR crystal up to temperatures of 400 K would cause scorching, while desintegration of the material was reported by [1] at 460 K. This too suggests that the experimental environment of the TIR setup compromises the sample's quality and therefore the value of the measurement results.

Transmission

Other than thin film growth options for sample preparation of optically dense materials include thin film slicing, or pressing pellets diluted with a IR transparent matrix like KBr. From the ATR spectra, the linear attenuation coefficient could be estimated:

$$A_{10} = -log_{10}(e^{-\alpha d_e}) \Rightarrow \alpha = \frac{A_{10}}{d_e \cdot log_{10}(e)} \tag{4}$$

Inserting the absorbance maxima from the ATR spectra 0.45 (PEA) and 0.60 (EA), and assuming an optimistic effective sampling depth of 10 μm gives:
$\alpha_{max} = 1.04 \cdot 10^5$ for (PEA)CuCl and $\alpha_{max} = 1.38 \cdot 10^5$ for (EA)CuCl.

For a 10% transmission, being a lower limit for detector linearity [15], this results in a required sample thickness of $d_{10} \approx 22\mu m$ for (PEA)CuCl and $d_{10} \approx 17\mu m$ for (EA)CuCl. Considering this estimation, the option of thin film growth on a substrate was chosen for practicality reasons. It was also assumed that a well grown thin film would be more reliable in in temperature dependent measurements than a mixed and pressed pellet sample. However, alternatives were not attempted and nothing can be said about their potential assets.
The possibility of preparing thin film samples of perovskite hybrids by quick evaporation on a substrate was described by reference [5]. In this case, the crystals were grown from an ethanol solution. To acquire extremely thin films (less than 20 μm), the lower solubility and quicker evaporation of ethanol compared to water was considered favourable. This procedure is much

less controlled than what is required for growing thicker single crystalline crystals. Since it is questionable whether the thin films possessed the desired crystal structure, a comparison was made of their low frequency Raman spectra with 'correctly' synthesized crystals. The modes recorded between 140 and 300 cm^{-1} have been ascribed to purely inorganic vibrations of the $CuCl_6$ octahedra [4]. Figure 25 shows a correspondence to some extent, though the actual structure should be confirmed by X-ray diffraction. Should the thin films indeed possess the desired structure, this would greatly increase the significance of the transmission measurements.

Figure 25: Raman spectra of (PEA)CuCl, (EA)CuCl and BaF samples

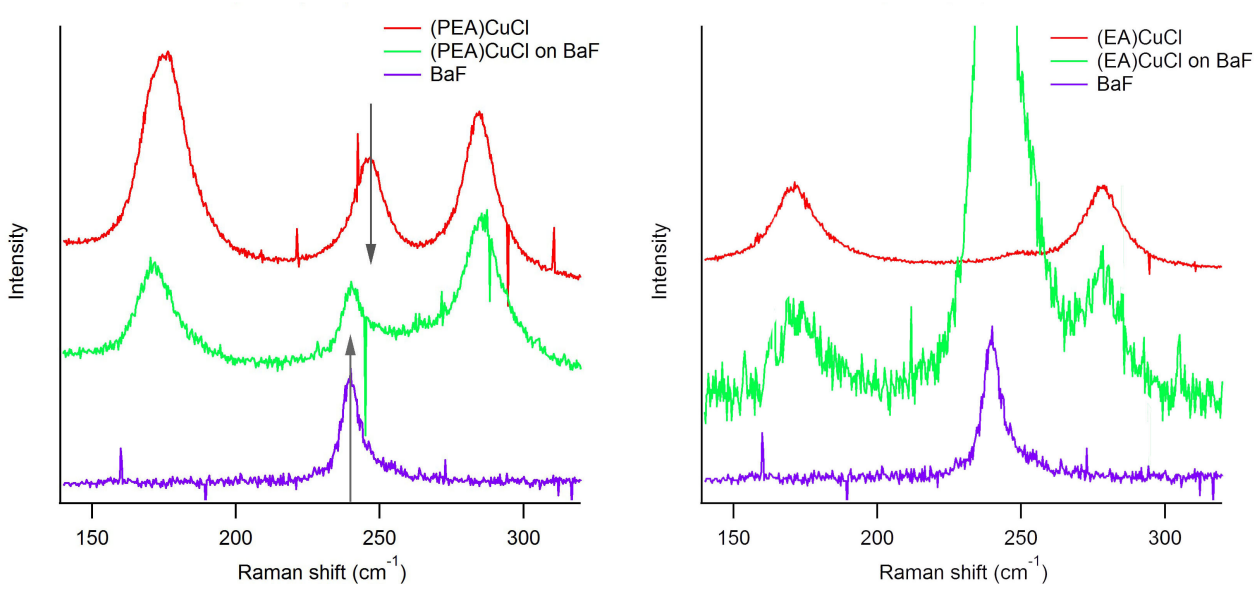

Comparison of the Raman spectra of (PEA)CuCl and (EA)CuCl. Red: crystals synthesized as described by [1] and used in TIR measurements. Green: thin film samples on BaF substrate from evaporation of ethanol solution. Blue: Raman spectrum of BaF.

8.3 Total internal reflection versus transmission IR spectroscopy

Differences between the spectra recorded by TIR and transmission are found as the absence of some lines in the transmission spectra and the non-overlapping of the broad 2900-3200 cm^{-1} band. The vibrations above 900 cm^{-1} should all be present, since they belong to vibrations of the organic molecule and are not unique to the crystal structure. It is therefore unlikely that crystal structure should affect the spectrum in this frequency region.
A fundamental difference that plays a role is that the evanescent wave is not a transverse wave, so that it may excite vibrations in any direction. In the tranmission setup, dipoles aligned in the longitudinal direction of the beam will not be excited. Another possible influence is the wavelength dependence of penetration depth of the evanescent wave. Since longer wavelengths penetrate deeper into the sample, the ATR signal at lower wavenumbers will be improved relative to the higher wavenumbers.

Figure 26: (PEA)CuCl: Room temperature ATR and transmission spectra

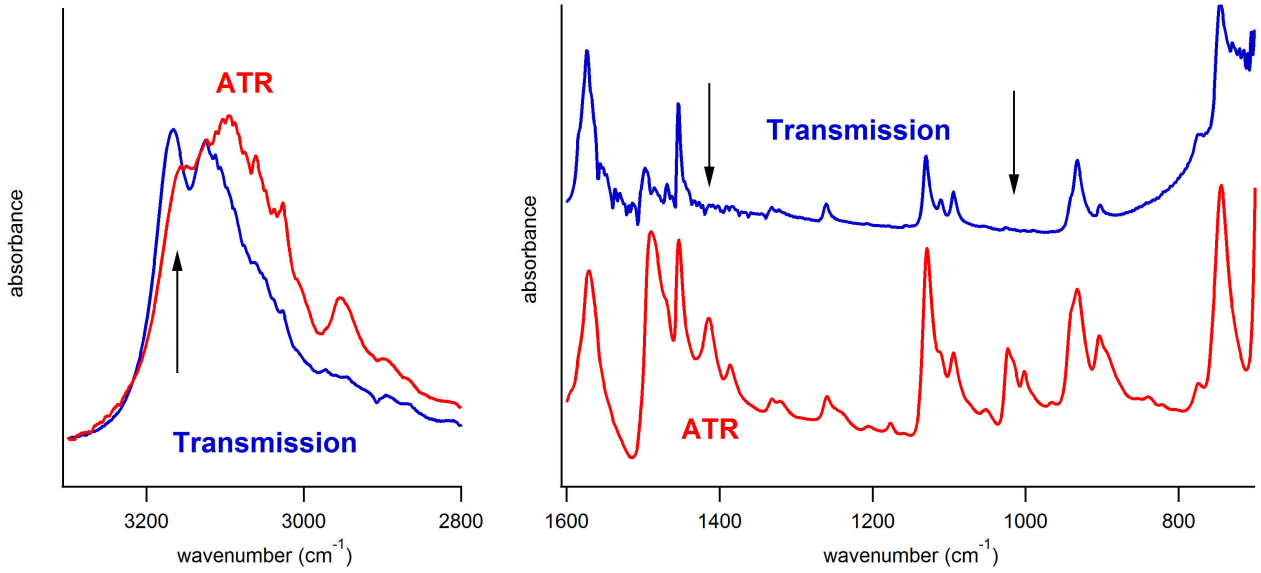

Figure 27: (EA)CuCl: Room temperature ATR and transmission spectra

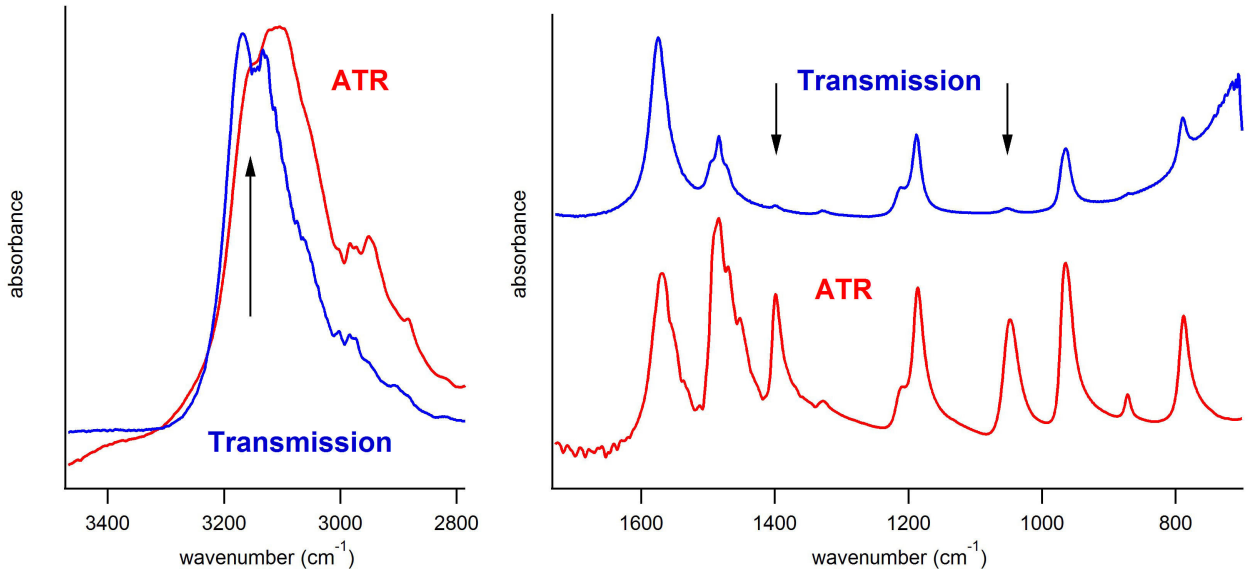

8.4 Propositions

In this section I will address a few issues in a somewhat different way. Throughout this thesis, I have attempted to to keep the words and data presented as meaningful as possible. However, the number of "gut feelings", ideas on the topic that lack solid explanations, might be equally meaningful as the few conclusions that do find ample support in the data. The following propositions can not be regarded as conclusive results, but are worth taking into consideration.

The polar phase transition does not significantly affect the hydrogen bond strengths to cause discernable shifts in the NH stretching frequencies. For now it may be too blunt to draw this

conclusion. But despite the fact that some aspects of the experiments are questionable, it is sensible to also consider the contrary. The hypothesis that the phase transition can be recognized in NH stretching vibrations requires that individual hydrogen bonds are loosened or tightened substantially at T_c. Whereas the positions of the NH_3 group and the $CuCl_6$ octahedra change to account for the (dis)appearance of the polarized phase, this does not necessarily imply that hydrogen bond lengths or strengths are equally affected.

The most promising sampling method of the hybrids in the mid-IR range is provided by Infrared transmission through thin films obtained by rapid evaporation of solution on a transparent substrate. How to deal with the high optical density of both (PEA)CuCl and (EA)CuCl in the 2900-3200 cm^{-1} range has been an important question in preparing a transmission experiment. A reasonable assumption was that the crystals should be treated respectfully in order to obtain reliable measurements. The TIR setup, in which samples are crushed onto the reflection element, and grinding the samples into KBr pellets are therefore considered undesirable. Although slicing of thin samples would be a good way, I expected the required (estimated) thickness of <20 μm to complicate the process. The thin film samples made may or may not possess the right crystal structure; this still needs confirmation. However, there is no reason to expect that good quality samples can be obtained this way quite easily.

The temperature dependent IR-spectra of the (EA)CuCl hybrid differ in some unexpected ways from to the (PEA)CuCl hybrid. In the beginning, there was the assumption that (EA)CuCl would behave similarly to (PEA)CuCl concerning the phase transition. The smaller organic molecule would also allow for an easier interpretation of its spectrum. In the data, the recorded spectra of (EA)CuCl add confusion rather than clarity.
Studying the NH vibrations in (EA)CuCl instead of (PEA)CuCl can still be regarded as an easier alternative, provided that their high temperature phase transitions are similar. The inconsistent (313 K - 373 K) and unexpected (80 K - 296 K) temperature dependence of the spectra should not discourage from switching the focus to this material, based on the much smaller number of high frequency vibrations.

9 Conclusion

It can safely be concluded that any sign of the high temperature phase transition in (PEA)CuCl in the high 2900-3200 cm^{-1} frequency region is too small to be resolved by the experimental methods used for this thesis. Further research on the materials by vibrational spectroscopy in this frequency region will necessarily require that the absorption lines affected by the phase transition can be resolved sufficiently. Alternatively, their significance must be disproven definitively. One way or another, both require an experiment with minimal error.
In this project, much time and effort has been invested in attempts to recognize the phase transition in temperature dependent TIR infrared measurements. Although simple and effective for recording qualitative aspects of the spectra, the experimental setup did not allow for fine temperature adjustments and careful treatment of the sample. Transmission measurements do allow for superior control of experimental conditions but also require extremely thin samples. For those used for the current measurements, the desired crystal structure could not be confirmed conclusively.
Along with minimal measurement error, a far more detailed dissection of the broad 2900-3200 cm^{-1} absorption band will be required for future elaborate experiments. Spectroscopy at low temperatures provides a much improved resolution of the spectral lines which will probably be helpful in identifying them.
A future fruitful spectroscopic study of the (PEA)CuCl and (EA)CuCl hybrids in the high frequency range will require:

- Confirmation of the desired crystal structure in the used samples (by X-ray diffraction) or an alternative method to produce reliable thin film samples. Making thin films by evaporation from solution probably is likely to be one of the simplest and most effective ways.
- A disctinction made between NH and CH vibrations in the spectrum, possibly by low temperature IR/Raman studies or making use of the NH_3 group's polar or hydrogen bonding properties.
- An IR-transmission experiment with minimal error at temperatures near T_c=340K.

Acknowledgements

In every possible way, working on this project has been an experience of "learing by doing". I would like to thank those people who have made it possible for me to learn what to do, how to do it and to also actually do it in the end:

Ben Hesp and Foppe de Haan for their endless support in setting up the measurements, providing practical answers and helping me to actually get things done;

Joop Vorenkamp (Technical support, RuG Polymer Science), for permitting use of the Bruker IFS-88 spectrometer, patiently explaining how to handle it and teaching me how to look at the data once I got them;

Rolf Versteeg for sharing his knowledge and experience on the hybrid materials, joining me in building the transmission setup and support in my first LATEX edited work;

Antonio Caretta for sharing his expertise on organic-inorganic hybrids and experimental methods;

Dr. Matteo Montagnese for teaching me the basics of IGOR Pro 6.1.2.1 to get going with the data analysis, as well as many thought provoking discussions on physics and virtually any other random subject;

Dr. Maxim Pchenitchnikov and prof.dr.ir. Paul van Loosdrecht for offering me this exciting project to work on, in nearly complete freedom to do experiments, make mistakes and get acquainted with academic research.

References

[1] A.H. Arkenbout. *Organic-Inorganic Hybrids - A Route wowards Soluble Magnetic Electronics*. PhD thesis, 2010.

[2] A.K. Cheetham, C.N.R. Rao, and R.K. Feller. Structural diversity and chemical trends in hybrid inorganic-organic framework materials. *Chem. Commun.*

[3] A.O. Polyakov, A.H. Arkenbout, and T.T.M. Palstra. Coexisting ferromagnetic and ferroelectric order in a $CuCl_4$-based organicinorganic hybrid. *Chem. Mater.*, 24:133–139, 2012.

[4] A. Caretta and P.H.M. van Loosdrecht. Low-frequency raman study of the ferroelectric phase transition in a layered $CuCl_4$-based organic-inorganic hybrid. In preparation.

[5] H. Arend, W. Huber, F. H. Mischgofsky, and G. K. Richter van Leeuwen. Layer perovskites: Importance, solubilities and simple growth techniques.

[6] M. Kozelj, R. Blinc, R. Kind, and G. Chapuis. ^{13}C NMR study of the bilayer phase transitions in $(C_{10}H_{21}NH_3)_2CuCl_4$. *J. Chem. Phys.*, 74:4123, 1980.

[7] V. Kapustianyk, Y. Korchak, and S. Dacko. Electron-phonon interaction and phase transitions in $(C_2H_5NH_3)_2CuCl_4$ crystals. *phys. stat. sol.*, 207:95, 1997.

[8] V. Kapustianyk, V. Rudyk, and M. Partyka. Visible spectroscopy study of the low dimensional $(C_2H_5NH_3)_2CuCl_4$ compound in the region of its low temperature phase transitions. *phys. stat. sol.*, 244, 2007.

[9] G. Heygster and W. Kleeman. Optical investigations on magnetic and structural phase transitions of $(CH_3NH_3)_2CuCl_4$ and $(C_2H_5NH_3)_2CuCl_4$. *Physica*, 89B, 1977.

[10] I. Bakaimi B. Kundys. Multiferroicity and hydrogen-bond ordering in $(C_2H_5NH_3)_2CuCl_4$ featuring dominant ferromagnetic interactions. *phys. review B*, 81, 2010.

[11] H. Kuzmany. *Solid-State Spectroscopy - An Introduction*, chapter Infrared Spectroscopy. Springer-Verlag, Berlin Heidelberg, 2009.

[12] F.M. Mirabella. Principles, theory and practice of internal reflection spectroscopy. In *Handbook of Vibrational Spectroscopy - Volume 2*. Wiley, 2002.

[13] C.N.R. Rao, S. Ganguly, and H.R. Swamy. Infrared studies of the phase transitions of alkylammonium halides and bis-(alkylammonium) tetrahalogenometallates. *J. Chem. Soc. Faraday Trans. 2*, 77:1825–1836, 1981.

[14] A.I. Fishman and A.B. Remizov. The vibrational spectra and conformations of ethylbenzene. *Spectrochimica Acta pt A*, 60, 2004.

[15] J.M. Chalmers. Mid-infrared spectroscopy: anomalies, artifacts and common errors. In *Handbook of Vibrational Spectroscopy - Volume 3*. Wiley, 2002.